Continuous and discrete microstructured materials with null Poisson's ratio

Giorgio Carta[a], Luigi Cabras[b], Michele Brun[c,*]

[a] *Department of Mathematical Sciences, University of Liverpool, UK*
[b] *Department of Solid and Structural Mechanics, University of Trento, Italy*
[c] *Department of Mechanical, Chemical and Materials Engineering, University of Cagliari, Italy*

Abstract

In this paper we propose different classes of isotropic microstructured media with tunable Poisson's ratio. The elastic periodic systems are continuous porous media and two- and three-dimensional lattices. The microstructural parameters can be tuned in order to have an effective Poisson's ratio equal to zero. The connection between microstructural parameters and effective properties is shown in detail both analytically and numerically.

Keywords: Null Poisson's ratio, porous materials, lattice structures, isotropic media, metamaterials

1. Introduction

The effective behavior of a material depends on the internal structure that is possessed by the material at different scales (see, for example, Christensen (1979) and Milton (2002)). The capability to design different microstructures can lead to extreme constitutive properties, that cannot be achieved by naturally occuring materials. In the last decades the design of new microstructured media has been accompanied by new technologies in the production of artificial materials, such as 3D printing, 3D laser and multiphoton litography, with possible advanced applications for ceramic materials, as shown by Bauer et al. (2014) and Jang et al. (2013).

In the present paper we are interested in the design of new microstructures, that can guarantee a Poisson's ratio equal to zero. The purpose of this

*Corresponding author
Email addresses: giorgio_carta@unica.it (Giorgio Carta), luigi.cabras@unitn.it (Luigi Cabras), mbrun@unica.it (Michele Brun)

choice is in the possibility of 'decoupling' the deformation mechanism in different directions, so that when a material is stressed in one direction it does deform only in the direction of the load, but not in the orthogonal directions. Another feature of interest is the design of isotropic materials, so that the 'decoupling deformation' mechanism does not depend on the direction of the application of the load.

For isotropic materials constitutive stability limits the Poisson's ratio ν between -1 and 0.5. While negative values of Poisson's ratio are theoretically possible, most of the naturally occuring materials show positive ν. Love (1944) mentioned materials with a negative Poisson ratio, which are named auxetic after Evans (1991). Extended reviews of existing auxetic models can be found in Greaves et al. (2011), Elipe et al. (2012), Mir et al. (2014), Milton (2015). There are very few examples of materials with null Poisson's ratio. A naturally occurring material with a Poisson's ratio close to zero is cork (Jardin et al. (2015)), while a three-dimensional spongy graphene and a nanoparticle multilayer have been proposed by Wu et al. (2015) and by Nguyen et al. (2012), respectively, as artificial systems with $\nu = 0$. Materials with null Poisson's ratio are very useful for sealing (Gibson and Ashby (1997)) and biomedical applications, such as scaffolds in tissue engineering (Soman et al. (2012)).

Here, we present different classes of microstructured materials: a porous continuum and different classes of lattices. The topology of the microstructure assures an isotropic behavior at least within the linear range of the stress-strain response curve of the material. The effective behavior can be tuned by modulating the microstructural parameters. The microstructure is simple and can be easily produced with existing technologies.

The paper is organized as follows. In Section 2 we present the porous medium and we give evidence of the effect of the size and of the relative inclination of the pores on the effective properties. In Section 3 we propose different lattice models, namely a two-dimensional lattice with a hexagonal and a triangular microstructure and a three-dimensional body centered cubic system. In the plane models effective properties are given analytically, while for the three-dimensional lattice the problem is analyzed numerically. For all the elastic systems analyzed we show the design of isotropic media with Poisson's ratio equal to zero. Final considerations conclude the paper.

2. A continuous porous model

We consider a perforated ceramic sheet, which can be designed such that it exhibits a null Poisson's ratio. The holes are disposed in a hexagonal arrangement as sketched in Fig. 1a, where θ is the angle measured from the

normal to the hexagon side and l is the hexagon side length. Each hole is made of a rectangle of length a, ending with two semicircles of diameter b, as shown in Fig. 1b. The structure is formed by repetitive cells, one of which is drawn in Fig. 1c.

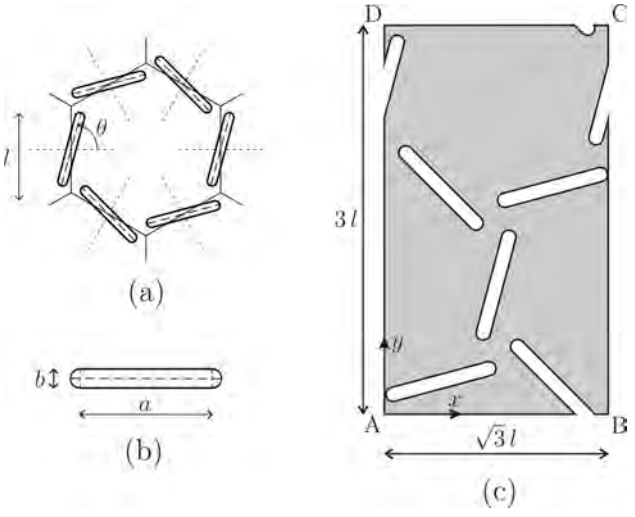

Figure 1: (a) Hexagonal pattern of the holes in the two-dimensional ceramic structure; (b) illustration of a single hole; (c) representation of the elementary cell of the structure.

We assume that the matrix is made of magnesium oxide, which is used in several engineering applications for its excellent performance at high temperatures, resistance to corrosion and transparency to infrared light. The matrix is characterised by a Young's modulus $E_m = 300\,\text{GPa}$, a Poisson's ratio $\nu_m = 0.36$ and a yield stress $\sigma_y = 160\,\text{MPa}$. The elastic modulus and Poisson's ratio of the homogenised structure, consisting of both the matrix and the holes, will be indicated as E and ν, respectively.

We note that the hexagonal disposition of the holes makes the medium isotropic in the plane (see Carta et al. (2015)). As a consequence, the constitutive properties of the perforated sheet can be evaluated by loading or stretching the structure in only one direction.

2.1. Finite structure

We start by analysing a perforated sheet of finite dimensions. The structure has a square shape of side $L = 200\,\text{mm}$ on the plane x-y, as shown in black color in Fig. 2a, with a thickness $t = 5\,\text{mm}$ in the z direction. The dimensions of the microstructure are the following: $l = 9.0\,\text{mm}$, $b = 1.0\,\text{mm}$, $a = 0.765\,l = 6.9\,\text{mm}$ and $\theta = 75°$.

We determine the homogenised properties of the perforated sheet by employing a finite element model developed in *Comsol Multiphysics*®. We use

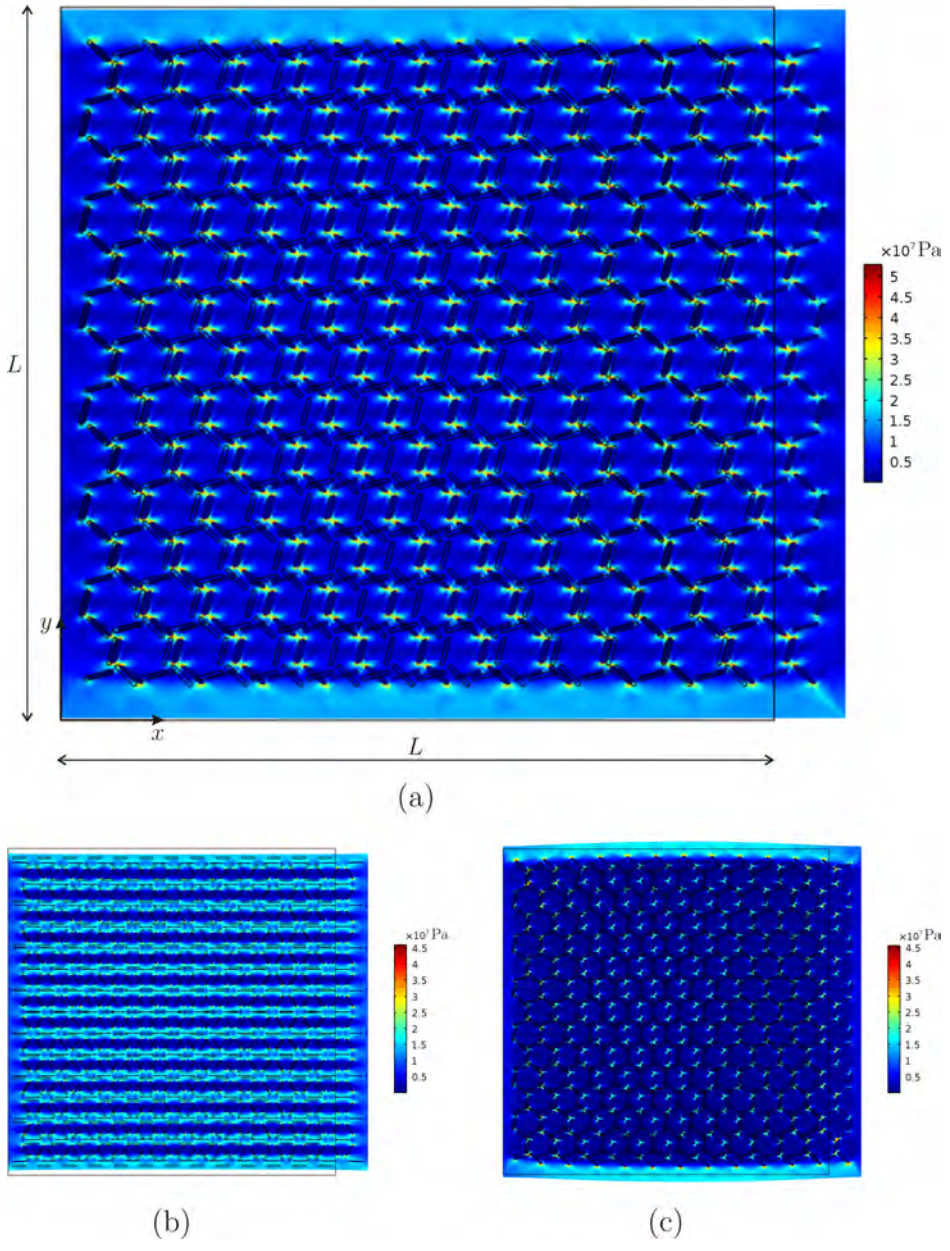

Figure 2: (a) Finite structure showing a null Poisson's ratio ($\theta = 75°$, $a/l = 0.765$); comparison with structures having the same matrix properties but different holes, exhibiting (b) a positive Poisson's ratio ($\theta = 0°$, $a/l = 0.765$) and (c) a negative Poisson's ratio ($\theta = 75°$, $a/l = 1.000$). The undeformed configurations are shown in black, while the colors in the deformed configurations represent the values of the von Mises stress, indicated on the right of each figure.

a mesh of around 5×10^5 triangular elements, which is refined near the holes.

We impose zero horizontal displacements at the left boundary and apply a horizontal displacement of 0.01 mm on the right boundary.

The deformed configuration in shown in Fig. 2a (in the figure, the scale factor for the displacement is equal to 2000). The colors indicate the values of the von Mises stress, which are detailed on the right of the figure. We point out that the maximum value of the von Mises stress, detected near the holes, is well below the yield limit σ_y of the matrix. From Fig. 2a it is apparent that the perforated sheet does not contract nor expand laterally as it is stretched, hence it has a null value of the Poisson's ratio.

In order to precisely compute the homogenised Poisson's ratio and Young's modulus of the porous structure, we refer to a square area of side 100 mm in the central part of the model. This area is far enough from the boundaries to neglect the boundary layer effects and it is large enough to contain a sufficient number of elementary cells. In this area, we determine the average normal stresses $\overline{\sigma}_{xx}$ and $\overline{\sigma}_{yy}$ and the average axial strains $\overline{\varepsilon}_{xx}$ and $\overline{\varepsilon}_{yy}$. The homogenised Poisson's ratio and elastic modulus are calculated from the following expressions:

$$\nu = \frac{\overline{\sigma}_{yy}\,\overline{\varepsilon}_{xx} - \overline{\sigma}_{xx}\,\overline{\varepsilon}_{yy}}{\overline{\sigma}_{xx}\,\overline{\varepsilon}_{xx} - \overline{\sigma}_{yy}\,\overline{\varepsilon}_{yy}}, \tag{1}$$

$$E = \frac{\overline{\sigma}_{xx}^2 - \overline{\sigma}_{yy}^2}{\overline{\sigma}_{xx}\,\overline{\varepsilon}_{xx} - \overline{\sigma}_{yy}\,\overline{\varepsilon}_{yy}}. \tag{2}$$

We obtain $\nu = -0.00156 \approx 0$ and $E = 81.3\,\mathrm{GPa}$. The Young's modulus of the porous structure is obviously smaller than that of the matrix for the presence of the holes.

If the orientation angle θ is modified while keeping the length of the holes a fixed, the behavior of the perforated sheet can be affected significantly. For instance, if $\theta = 0^\circ$ the porous structure exhibits a positive Poisson's ratio (see Fig. 2b). On the other hand, if the value of θ is not changed whereas a is increased, the Poisson's ratio of the medium becomes negative (see Fig. 2c). The deformations of the porous structure under stretching and compression in the three different cases investigated in Fig. 2 are better illustrated in the videos accompanying this paper (see Video1-Video3 in the Supplementary Material).

2.2. Periodic structure

Now we assume that the perforated sheet is of infinite extent, so that we can study a single elementary cell with periodic conditions at the boundaries. We determine the homogenised properties of the cell by applying a macroscopic uniaxial strain $\overline{\varepsilon}_{xx} = 10^{-4}$, which is below the yield limit. Accordingly,

the periodic conditions are given as follows (refer to Fig. 1c):

$$u|_{\mathrm{BC}} = u|_{\mathrm{AD}} + \overline{\varepsilon}_{xx}\sqrt{3}\,l, \quad v|_{\mathrm{BC}} = v|_{\mathrm{AD}}\,, \quad u|_{\mathrm{CD}} = u|_{\mathrm{AB}}\,, \quad v|_{\mathrm{CD}} = v|_{\mathrm{AB}}\,. \tag{3}$$

In the formulae above, u and v are the horizontal and vertical components of the displacement field, respectively. In order to compute the average values of the normal stresses $\overline{\sigma}_{xx}$ and $\overline{\sigma}_{yy}$, we build a finite element model in *Comsol Multiphysics*®, which has a very fine mesh with around 25000 triangular elements. Then, we calculate the homogenised Poisson's ratio ν and Young's modulus E from Eqs. (1) and (2), respectively. We find $\nu = 0.00132 \approx 0$ and $E = 83.1\,\mathrm{GPa}$, which are very close to the values obtained for the finite structure (the small discrepancies are due to the boundary layer effects). The same results are derived by applying a macroscopic uniaxial strain $\overline{\varepsilon}_{yy} = 10^{-4}$ or a macroscopic shear strain $\overline{\varepsilon}_{xy} = 10^{-4}$, since the medium is isotropic in the plane.

The periodic elementary cell is adopted to perform a parametric study on the geometrical and constitutive properties of the structure. For instance, it is interesting to investigate the effects of the orientation angle θ on the behavior of the medium. To this aim, we fix the elastic constants of the matrix ($E_m = 300\,\mathrm{GPa}$, $\nu_m = 0.36$) and we determine - for different values of the orientation angle θ - the ratio a/l which yields a null Poisson's ratio. The outcomes are shown in Fig. 3a by the circles, while the squares represent the limit values of the ratio a/l, above which the holes merge. In Fig. 3b we report the corresponding values of the homogenised Young's modulus. As expected, the porous structure achieves the maximum rigidity when the length of the holes has a minimum, found at $\theta = 52.5°$. This result is very important for practical applications to optimise the mechanical behavior of the structure.

Next, we fix the value of the inclination angle and of the Young's modulus of the matrix ($\theta = 52.5°$, $E_m = 300\,\mathrm{GPa}$) and we consider different values of the Poisson's ratio of the matrix ν_m. For each value of ν_m, we compute the ratio a/l that gives $\nu = 0$. The results are plotted in Fig. 4a, while Fig. 4b shows the relative values of the homogenised elastic modulus. The ratio a/l increases with ν_m, with a trend that is almost linear; nonetheless, the range of variation of a/l is narrow. Correspondingly, as a/l increases the homogenised Young's modulus E decreases.

Finally, we set $\theta = 52.5°$ and $\nu_m = 0.36$, and we vary E_m. For each value of E_m, we determine the ratio a/l which provides $\nu = 0$, shown in Fig. 4c. As expected, the change in the elastic modulus of the matrix does not affect the ratio a/l for which $\nu = 0$, which remains constant ($a/l = 0.710$). Fig. 4d shows the corresponding values of the homogenised elastic modulus E, which increases linearly with E_m.

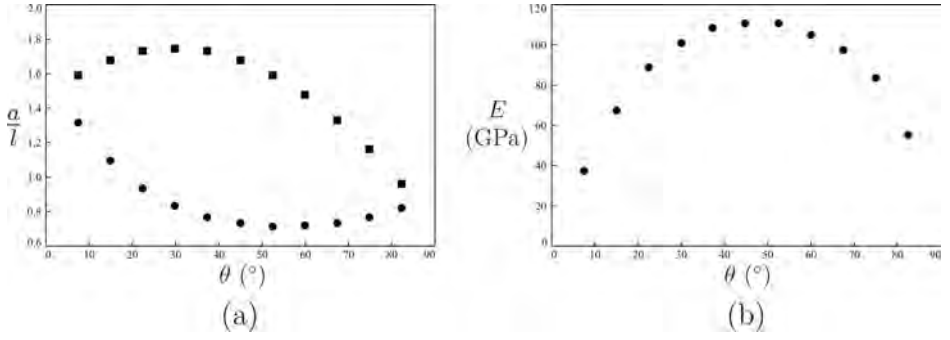

Figure 3: (a) Circles: values of a/l for which the perforated sheet has a null Poisson's ratio, for different values of the inclination angle θ; squares: maximum values of a/l, beyond which the holes coalesce. (b) Corresponding values of the homogenised Young's modulus E. In these computations, we have taken $E_m = 300\,\mathrm{GPa}$ and $\nu_m = 0.36$.

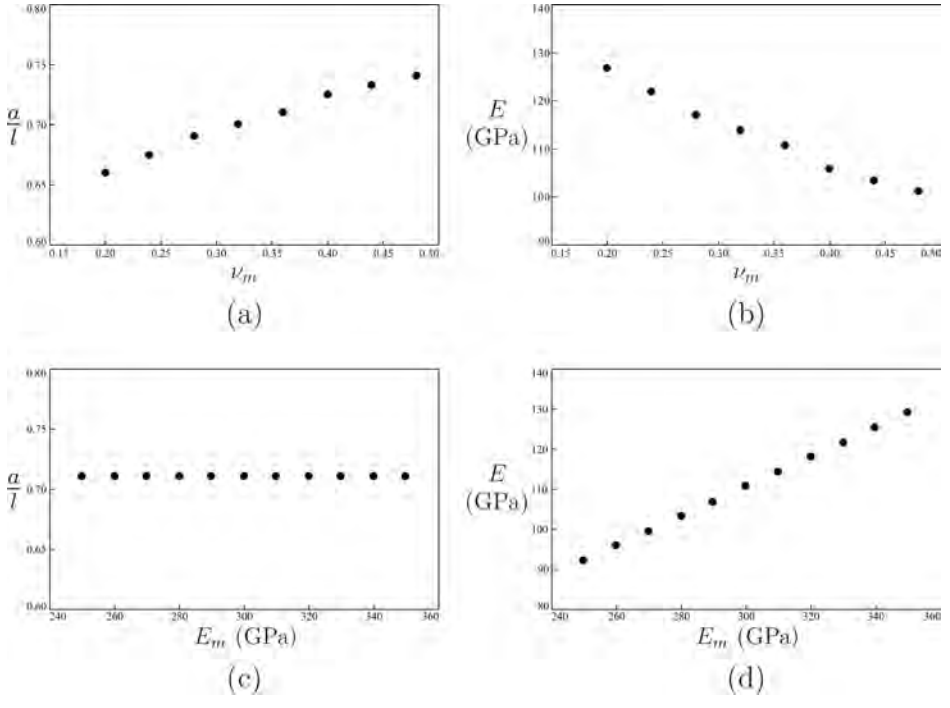

Figure 4: (a) Values of a/l for which $\nu = 0$, determined for different values of the Poisson's ratio of the matrix ν_m; (b) corresponding values of the Young's modulus E ($\theta = 52.5°$, $E_m = 300\,\mathrm{GPa}$). (c) Values of a/l for which $\nu = 0$, derived for several values of the elastic modulus of the matrix E_m; (d) corresponding values of the homogenised Young's modulus E ($\theta = 52.5°$, $\nu_m = 0.36$).

The macroscopic behavior and, in particular, the Poisson's ratio is affected slightly by a variation of the hole width b, assuming that the latter is much smaller than the hole length, namely $b/a \ll 1$.

3. Lattice models

We propose a class of isotropic lattices, which are designed to exhibit a Poisson's ratio equal to zero. This effect is achieved by the superposition of clockwise and anti-clockwise internal rotations leading to a macroscopic non-chiral effect. Two in-plane isotropic lattices and a three-dimensional isotropic lattice are proposed, for which the macroscopic Poisson's ratio is given as a function of the constitutive behaviors of the single constituents and of the micro-structure. For the two-dimensional lattices we determine analytically the properties capable to guarantee a null Poisson's ratio, whereas for the three-dimensional lattice the results are obtained numerically implementing a finite element model.

3.1. Two-dimensional lattices

The two-dimensional lattices are composed of cross-shaped elements with arms of the same length p (see Fig. 5). The number of arms is 3 and 6 for the hexagonal and the triangular geometries, respectively. The lattices are built by assembling each couple of cross-shaped elements in two parallel planes; indicated in blue and red in Fig. 5. Each couple is mutually constrained to have the same displacement at the central point, where a hinge is introduced. Different couples are then constrained at the external end of each arm by truss elements acting as longitudinal springs. The springs, with longitudinal stiffness k_L, are depicted in green in Fig. 5. The three-fold and six-fold symmetries of the microstructures assure an isotropic behavior if the blue and red cross-shaped elements have the same material properties (see Cabras and Brun (2014)). We restrict the attention to the linear elastic range. The linearized behavior depends nonlinearly on the reference configuration described by the angle γ between the arms and the springs (see Fig. 5).

The two geometries described in Fig. 5 correspond to the fundamental centered rectangular (rhombic) and hexagonal Bravais lattices, respectively. The periodic systems have a Bravais periodic lattice

$$\mathbf{R} = n_1\mathbf{t}_1 + n_2\mathbf{t}_2\,, \tag{4}$$

where $n_{1,2}$ are integers and $\mathbf{t}_{1,2}$ are the primitive vectors spanning the lattice. For the hexagonal structure

$$\mathbf{t}_1 = p\,\sin\gamma \begin{pmatrix} 0 \\ 6 \end{pmatrix}, \qquad \mathbf{t}_2 = p\,\sin\gamma \begin{pmatrix} -\sqrt{3} \\ 3 \end{pmatrix}, \tag{5}$$

while for the triangular one

$$\mathbf{t}_1 = p\,\sin\gamma \begin{pmatrix} 0 \\ 1 \end{pmatrix}, \qquad \mathbf{t}_2 = p\,\sin\gamma \begin{pmatrix} -\sqrt{3}/2 \\ -1/2 \end{pmatrix}. \tag{6}$$

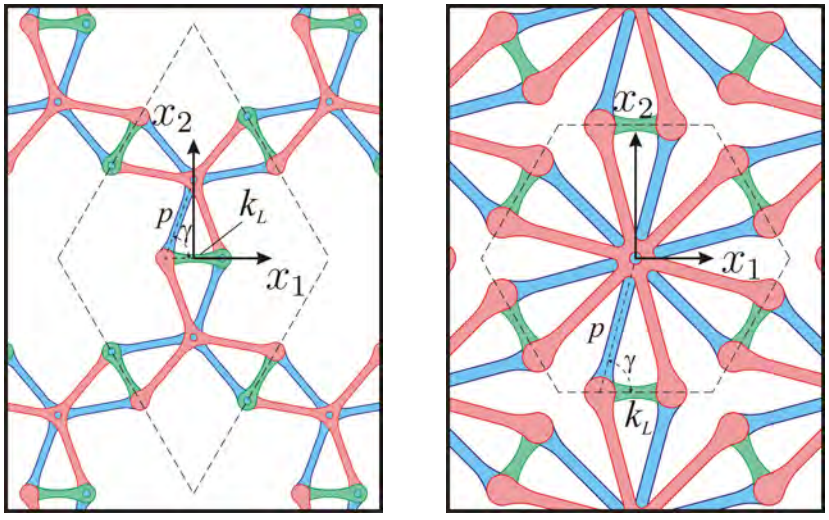

(a) (b)

Figure 5: Lattice composed of cross-shaped elements, depicted in blue and red, and elastic trusses, depicted in green. The longitudinal stiffness of the trusses is k_L. (a) Hexagonal lattice, (b) triangular lattice. The dashed area represents a typical unit cell of the periodic elastic system.

In order to determine the effective properties of the lattices, we implement classical structural theories considering each arm of a single cross-shaped element as an Euler-Bernoulli beam undergoing flexural and longitudinal deformations. The beams have Young's modulus E_b, cross-sectional area A_b and second moment of inertia J_b. The truss elements (depicted in green in Fig. 5) have longitudinal stiffness equal to k_L. We introduce the non-dimensional stiffness ratio parameters $\alpha_1 = k_L p/(E_b A_b)$ and $\alpha_2 = k_L p^3/(E_b J_b)$. Periodic boundary conditions are considered; in particular, we apply antiperiodic nodal forces indicated with F_N, F_{T_1} and F_{T_2} in Fig. 6a and additional kinematic constraints to prevent rigid body motions. The macroscopic stresses are computed averaging the resultant forces on the boundary of the unit cell.

The macroscopic effective properties are computed analytically by means of the Principle of Virtual Work (PVW), that is applied in two steps. In the first step we find the internal actions (bending moments M, shear forces V, axial forces N and spring forces S) of the structure searching for the kinematically admissible configuration in the set of statically admissible ones (*Flexibility Method*, see Capurso (1971)). In the second step we compute the macroscopic displacements. In the following, we describe in detail the determination of the effective properties for the hexagonal microstructure.

We consider the elastic structure as in Fig. 6a, subjected to known normal and tangential external forces. Forces F_N and $F_T = (F_{T_1} + F_{T_2})/2$ are

associated with macroscopic stresses

$$\overline{\sigma}_{11} = \frac{\sqrt{3}F_N + F_T}{3p\sin\gamma}, \quad \overline{\sigma}_{22} = \frac{\sqrt{3}F_N - 3F_T}{3p\sin\gamma}. \tag{7}$$

We introduce an equivalent statically determined (or isostatic) system as in

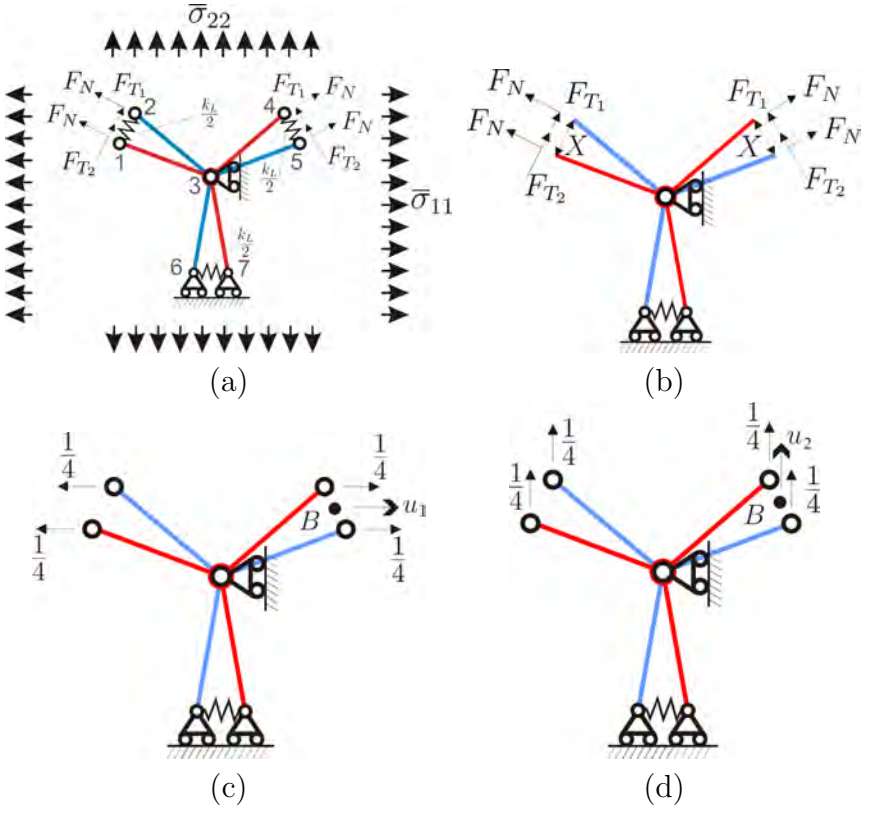

Figure 6: Simplified lattice structures used in the Principle of Virtual Work. (a) Simplified structure, where the reaction forces F_N, F_{T_1} and F_{T_2}, with $F_T = (F_{T_1} + F_{T_2})/2$ correspond to macroscopic stress components $\overline{\sigma}_{11}$ and $\overline{\sigma}_{22}$ as in eq. (7). Grey numbers in part (a) indicate the nodes. (b) Disconnected statically determined structure introduced for the determination of the internal actions M, N and S. Structures adopted for the computation of the horizontal displacement u_1 (c) and the vertical displacement u_2 (d) of the point B.

Fig. 6b, where the force in the springs X is the unknown to be determined. The general field of tension Λ ($\Lambda = M, V, N, S$) in equilibrium with the external loads is

$$\Lambda = \Lambda_0 + X\Lambda_1, \tag{8}$$

where the field Λ_0 is due to the external loads, while Λ_1 is the autosolution of the problem, computed with zero external loads and $X = 1$. The expressions of the internal actions are reported in Table 1 for each beam. The unknown

Beam	Axial force N	Bending moment M
23	$N_0 = \frac{(2\cos^2\gamma+1)F_N-\sqrt{3}F_T}{\sin\gamma}$ $N_1 = -2\cos\gamma$	$M_0 = 2\,F_N\cos\gamma\,x$ $M_1 = -2\sin\gamma\,x$
34	$N_0 = F_T\cos\gamma + F_N\sin\gamma$ $N_1 = \cos\gamma$	$M_0 = -F_T\sin\gamma\,x + F_N\cos\gamma\,x$ $M_1 = -\sin\gamma\,x$
37	$N_0 = -F_T\cos\gamma + F_N\sin\gamma$ $N_1 = \cos\gamma$	$M_0 = -F_T\sin\gamma\,x - F_N\cos\gamma\,x$ $M_1 = \sin\gamma\,x$
13	$N_0 = \frac{F_N\cos 2\gamma+2F_N-F_T\sqrt{3}}{\sin\gamma}$ $N_1 = -2\cos\gamma$	$M_0 = 2\,F_N\cos\gamma\,x$ $M_1 = -2\sin\gamma\,x$
36	$N_0 = -F_T\cos\gamma + F_N\sin\gamma$ $N_1 = \cos\gamma$	$M_0 = -F_T\ \sin\gamma\,x - F_N\cos\gamma\,x$ $M_1 = \sin\gamma\,x$
35	$N_0 = F_T\cos\gamma + F_N\sin\gamma$ $N_1 = \cos\gamma$	$M_0 = -F_T\sin\gamma\,x + F_N\cos\gamma\,x$ $M_1 = -\sin\gamma\,x$

Spring force S	
$S_0 = \frac{-\sqrt{3}\,F_T\cos\gamma+3\,F_N\cos\gamma}{\sin\gamma}$	$S_1 = -2$

Table 1: Internal actions in the hexagonal lattice. Refer to Fig. 6a for the node numbers, indicating the starting and ending point of each beam.

X is computed as

$$X = -\frac{\sum_{beam}\int_0^p \left(M_0\frac{M_1}{EJ} + N_0\frac{N_1}{EA}\right)ds + \sum_{spring} S_0\frac{S_1}{k_L/2}}{\sum_{beam}\int_0^p \left(M_1\frac{M_1}{EJ} + N_1\frac{N_1}{EA}\right)ds + \sum_{spring} S_1\frac{S_1}{k_L/2}} = \\ = \left(F_N - \frac{\sqrt{3}(1+\alpha_1)}{3+3\alpha_1\cos^2\gamma+\alpha_2\sin^2\gamma}F_T\right)\mathrm{cotg}\gamma. \tag{9}$$

The external applied forces F_N and $F_T = (F_{T_1} + F_{T_2})/2$ are

$$F_T = \frac{3}{2}\frac{k_L p\sqrt{3}\sin\gamma(\sin^2\gamma\alpha_2 + 3\cos^2\gamma\alpha_1 + 3)(\overline{\varepsilon}_{11} - \overline{\varepsilon}_{22})}{2\sin^4\gamma\alpha_2^2 + 9\cos^4\gamma\alpha_1^2 + 3(2\sin^2\gamma\cos^2\gamma + 1)\alpha_1\alpha_2 + 3\alpha_2 + 9\alpha_1}, \tag{10}$$

$$F_N = \frac{1}{2}\frac{k_L p\sin\gamma(c_1\alpha_1^2 + c_2\alpha_2\alpha_1 + c_3\alpha_1 + c_4\alpha_2^2 + c_5\alpha_2 + 3c_6)\overline{\varepsilon}_{11}}{c_{11}\alpha_1^3 + c_{10}\alpha_1\alpha_2^2 + c_{12}\alpha_1^2\alpha_2 + c_{13}\alpha_2^2 + c_{14}\alpha_1^2 + c_{15}\alpha_1\alpha_2 + 3c_6\alpha_1 + c_6\alpha_2} + \\ + \frac{k_p\sin\gamma(c_7\alpha_1^2 + c_8\alpha_1\alpha_2 + c_9\alpha_1 + c_4\alpha_2^2 + 3c_{10}\alpha_2 - 3c_6)\overline{\varepsilon}_{22}}{c_{11}\alpha_1^3 + c_{10}\alpha_1\alpha_2^2 + c_{12}\alpha_1^2\alpha_2 + c_{13}\alpha_2^2 + c_{14}\alpha_1^2 + c_{15}\alpha_1\alpha_2 + 3c_6\alpha_1 + c_6\alpha_2}, \tag{11}$$

respectively, where

$$
\begin{aligned}
&c_1 = 9(\sin^2\gamma\cos^4\gamma + \cos^2\gamma), && c_2 = 6(1+\cos^6\gamma - 2\cos^4\gamma),\\
&c_3 = -9(\sin^2\gamma\cos^2\gamma - 2), && c_4 = \sin^6\gamma,\\
&c_5 = -3(\cos^4\gamma - 1), && c_6 = 3\cos^2\gamma,\\
&c_7 = 9(\sin^2\gamma\cos^4\gamma - \cos^2\gamma), && c_8 = 6\sin^4\gamma\cos^2\gamma,\\
&c_9 = -9(\cos^4\gamma + \cos^2\gamma), && c_{10} = \sin^4\gamma,\\
&c_{11} = 9\cos^4\gamma, && c_{12} = 3(2\sin^2\gamma\cos^2\gamma + 1),\\
&c_{13} = \sin^4\gamma\cos^2\gamma, && c_{14} = 9(\cos^6\gamma + 1),\\
&c_{15} = 3(2\sin^2\gamma\cos\gamma^4 + \cos\gamma^2 + 1). &&
\end{aligned} \tag{12}
$$

Applying the superposition principle, as in eq. (8), the internal actions are given as linear functions of external forces F_N and F_T.

A second application of the PVW is performed in order to obtain the macroscopic displacement as linear combination of the external forces. The macroscopic displacement coincides with the displacement of the point B shown in Fig. 6c. To this purpose, we consider the real structure as kinematically admissible, and the isostatic structures, shown in Figs. 6c and 6d, as statically admissible. As a consequence, the PVW equations have the form

$$
u_i = \sum_{beam} \int_0^p \left(M_i^* \frac{M}{EJ} + N_i^* \frac{N}{EA} \right) d\xi + \sum_{spring} S_i^{L*} \frac{S}{k_L/2}, \quad (i = 1, 2), \tag{13}
$$

where (M_i^*, N_i^*, S_i^{L*}) $(i = 1, 2)$ are the internal actions of the statically admissible structure. We note that the virtual external work, i.e. the left hand side of eq. (13), coincides with the horizontal and vertical displacements of the point B, given by u_1 and u_2, respectively. The latter are obtained as

$$
\begin{aligned}
u_1 &= A_1\, F_N + B_1\, F_T,\\
u_2 &= A_2\, F_N + B_2\, F_T,
\end{aligned} \tag{14}
$$

where

$$
\begin{aligned}
A_1 &= \frac{\sqrt{3}(\alpha_1 + \cos^2\gamma)}{2\sin^2\gamma\, k_L},\\
B_1 &= \frac{9\cos^2\gamma(\cos^2\gamma\sin^2\gamma - 1)\alpha_1^2 - 9\cos^2\gamma(\cos^2\gamma + 1)\alpha_1}{6\sin^2\gamma(3 + 3\alpha_1\cos^2\gamma + \alpha_2\sin^2\gamma)k_L}\\
&\quad + \frac{6\cos^2\gamma\sin^4\gamma\,\alpha_1\alpha_2 + \sin^6\gamma\,\alpha_2^2 + 3\sin^4\gamma\,\alpha_2 - 9\cos^4\gamma}{6\sin^2\gamma(3 + 3\alpha_1\cos^2\gamma + \alpha_2\sin^2\gamma)k_L},
\end{aligned}
$$

$$A_2 = 3\frac{3\sqrt{3}\cos^2\gamma\,\alpha_1^2 + \sin^2\gamma\,\alpha_1\alpha_2 + 3(1+\cos^4\gamma)\alpha_1}{2\sin^2\gamma(3+3\alpha_1\cos^2\gamma+\alpha_2\sin^2\gamma)k_L}$$
$$+ 3\frac{\cos^2\gamma\sin^2\gamma\,\alpha_2 + 3\cos^2\gamma}{2\sin^2\gamma(3+3\alpha_1\cos^2\gamma+\alpha_2\sin^2\gamma)k_L},$$
$$B_2 = -\sqrt{3}\frac{9\cos^2\gamma(\cos^2\gamma\sin^2\gamma+1)\alpha_1^2+6\sin^2\gamma(\cos^2\gamma\sin^2\gamma+1)\alpha_1\alpha_2}{6\sin^2\gamma(3+3\alpha_1\cos^2\gamma+\alpha_2\sin^2\gamma)k_L}$$
$$- \frac{9(2-\cos^2\gamma\sin^2\gamma)\alpha_1 + \sin^6\gamma\,\alpha_2^2+3(1-\cos^4\gamma)\alpha_2+9\cos^2\gamma}{6\sin^2\gamma(3+3\alpha_1\cos^2\gamma+\alpha_2\sin^2\gamma)k_L}. \qquad (15)$$

The displacement components of point B are associated with the macroscopic strains

$$\overline{\varepsilon}_{11} = \frac{2u_1}{\sqrt{3}p\sin\gamma} = 2\frac{A_1F_N + B_1F_T}{\sqrt{3}p\sin\gamma}, \quad \overline{\varepsilon}_{22} = \frac{2u_2}{3p\sin\gamma} = 2\frac{A_2F_N + B_2F_T}{3p\sin\gamma}. \qquad (16)$$

Solving eqs. (16) in terms of F_N and F_T and substituting the results into eq. (7) leads to the effective constitutive relation between the macroscopic stress $\overline{\sigma}$ and macroscopic strain $\overline{\varepsilon}$, that can be used to determine the effective properties of the microstructured medium. The effective Poisson's ratio of the hexagonal lattice is found to be

$$\nu_{H_L} = \frac{\overline{\sigma}_{22}\overline{\varepsilon}_{11} - \overline{\sigma}_{11}\overline{\varepsilon}_{22}}{\overline{\sigma}_{11}\overline{\varepsilon}_{11} - \overline{\sigma}_{22}\overline{\varepsilon}_{22}} = \frac{c_1\alpha_1^2 + c_2\alpha_2^2 + c_3\alpha_1\alpha_2 + c_4\alpha_1 + c_5\alpha_2 + c_6}{c_7\alpha_1^2 + c_2\alpha_2^2 + c_8\alpha_1\alpha_2 + c_9\alpha_1 + c_{10}\alpha_2 - c_6}, \qquad (17)$$

where

$$\begin{aligned}
&c_1 = 9\cos^2\gamma(\cos^4\gamma - \cos^2\gamma + 2), && c_2 = -\sin^6\gamma,\\
&c_3 = 3\sin^2\gamma(2\cos^4\gamma - 2\cos^2\gamma + 1), && c_4 = 9(2\cos^4\gamma + \cos^2\gamma + 1)\\
&c_5 = -3(2\cos^4\gamma - 3\cos^2\gamma + 1), && c_6 = 18\cos^2\gamma,\\
&c_7 = 9\cos^2\gamma(\cos^4\gamma - \cos^2\gamma - 2), && c_8 = 3\sin^2\gamma(2\cos^4\gamma - 2\cos^2\gamma - 3),\\
&c_9 = -9(2\cos^4\gamma - \cos^2\gamma + 3), && c_{10} = -3\sin^2\gamma(2\cos^2\gamma + 1). \qquad (18)
\end{aligned}$$

We note that the effective Poisson's ratio depends on the stiffness ratios α_1, α_2 and on the geometric parameter γ.

In order to have a null Poisson's ratio we set to zero the numerator of the expression on the right hand side of eq. (17) and we solve it in terms of the stiffness ratio α_2. The condition of null Poisson's ratio is as follows:

$$\alpha_2 = 2\frac{1 - 2\sin^2\gamma + \alpha_1(1 - 2\sin^2\gamma + 2\sin^4\gamma) + (1+\alpha_1)|1 - 2\sin^2\gamma|}{3\sin^4\gamma}. \qquad (19)$$

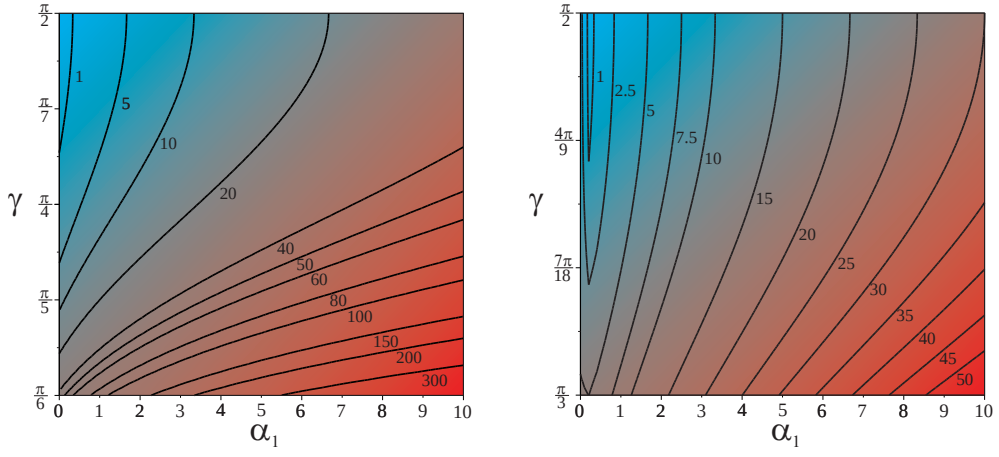

(a) (b)

Figure 7: Non-dimensional bending stiffness ratio α_2 as a function of the non-dimensional axial stiffness ratio α_1 and of the angle γ, in order to have zero effective Poisson's ratio. (a) Hexagonal lattice, eq. (19). (b) Triangular lattice, eq. (22).

In Fig. 7a we show the non-dimensional axial stiffness ratio α_2 as a function of the non-dimensional bending stiffness ratio α_1 and the angle γ that guarantees an effective Poisson's ratio ν=0, obtained from eq. (19).

For the triangular lattice the effective Poisson's ratio is given by

$$\nu_{T_L} = \frac{d_1\alpha_1^3 - 3\alpha_1^2\alpha_2 + d_2\alpha_1\alpha_2^2 + d_3\alpha_1^2 + d_4\alpha_2^2 + d_5\alpha_1\alpha_2 + d_6\alpha_1 + d_7\alpha_2}{-d_1\alpha_1^3 + d_8\alpha_1^2\alpha_2 + 3d_2\alpha_1\alpha_2^2 + d_9\alpha_1^2 + 3d_4\alpha_2^2 + d_{10}\alpha_1\alpha_2 - d_6\alpha_1 - d_7\alpha_2}, \tag{20}$$

where

$$\begin{aligned}
d_1 &= -9\cos^4\gamma, & d_2 &= \sin^4\gamma,\\
d_3 &= 9(\cos^6\gamma - 4\cos^4\gamma + 2\cos^2\gamma - 1), & d_4 &= \sin^4\gamma\cos^2\gamma,\\
d_5 &= 3(6\cos^4\gamma - 7\cos^2\gamma - 2\cos^6\gamma + 1), & d_6 &= -9\cos^2\gamma,\\
d_7 &= -3\cos^2\gamma, & d_8 &= 3(4\sin^2\gamma\cos^2\gamma + 1),\\
d_9 &= 9(3\cos^6\gamma - 4\cos^4\gamma + 2\cos^2\gamma + 1) & d_{10} &= 3(10\cos^4\gamma - 6\cos^6\gamma - 5\cos^2\gamma + 3).
\end{aligned} \tag{21}$$

In this case the condition leading to zero effective Poisson's ratio is

$$\alpha_2 = 3\frac{\cos^2\gamma + (1 + \cos^2\gamma - 2\sin^6\gamma)\alpha_1 + \alpha_1^2 + (1+\alpha_1)\sqrt{D}}{2\sin^4\gamma(1 + \alpha_1 - \sin^2\gamma)}, \tag{22}$$

where

$$D = \alpha_1^2 - 2\alpha_1\cos^2\gamma + (1 + 16\alpha_1 + 4\alpha_1^2)\cos^4\gamma + (20\alpha_1 + 8\alpha_1^2)\cos^6\gamma + (8\alpha_1 + 4\alpha_1^2)\cos^8\gamma. \tag{23}$$

In Fig. 7b we show α_2 versus the stiffness ratio α_1 and the angle γ, calculated from eq. (22), which assures an effective Poisson's ratio equal to zero.

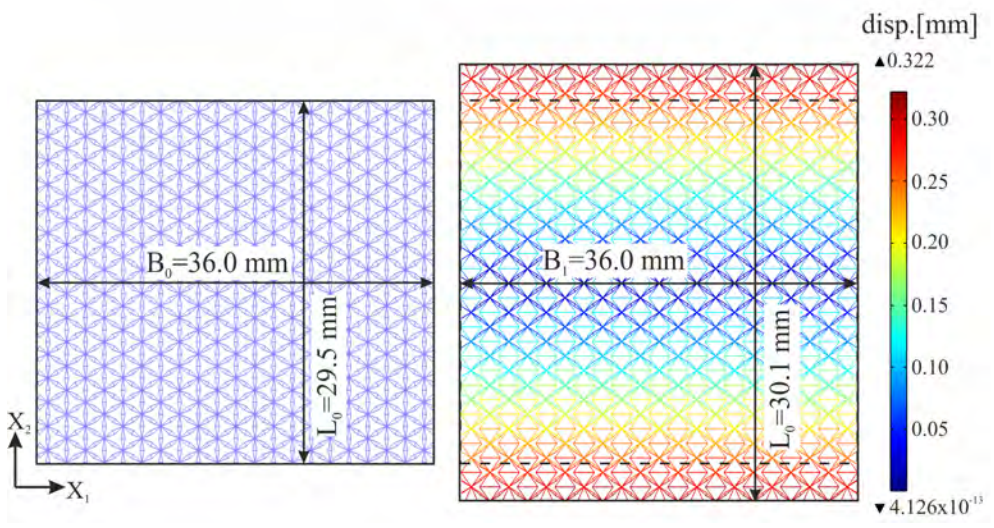

Figure 8: Triangular lattice subjected to an external uniaxial load along the direction x_2. The stress-free reference configuration is shown on the left, while the deformed configuration is plotted on the right. The dashed area in the picture on the right indicates the domain occupied by the undeformed configuration.

In Fig. 8 we show a the central part of a finite sample made up of 1005 triangular unit cells. The sample is subjected to an uniaxial external load applied in the vertical direction x_2. The Poisson's ratio is zero, as shown by the absence of horizontal deformations along the direction x_1 in the deformed configuration.

3.2. Three-dimensional lattice

We extend the study to a three-dimensional model that can lead to zero effective Poisson's ratio. We tessellate the space starting from the cubic cell shown in Fig. 9 as in Cabras and Brun (2015). Square cross-shaped elements, depicted in blue and black, are disposed on the faces of the cube and joined by a hinge at their central points, as in the two-dimensional lattice structures. Additional truss elements are introduced in order to give constitutive stability to the lattice. There are two types of additional ligaments: the first ones are trusses placed on the edges of the cube indicated in green in Fig. 9, the second ones are diagonal elements indicated in violet. By modulating the longitudinal stiffnesses of the two types of trusses it is possible to achieve first isotropic behavior and second an effective Poisson's ratio equal to zero.

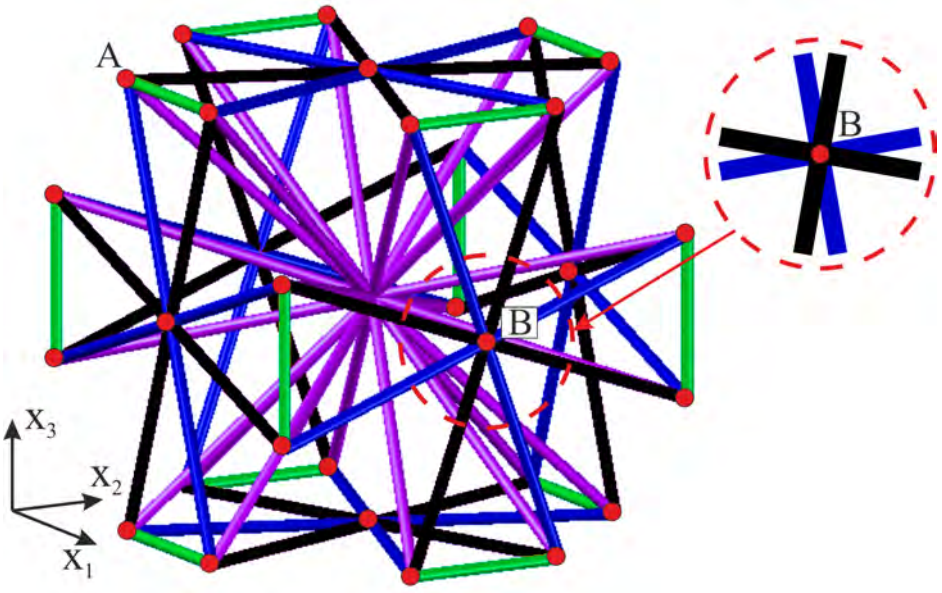

Figure 9: Three-dimensional cubic unit cell.

All the elements of the microstructure have Young's modulus E_m and Poisson's ratio ν_m. The arms of the cross-shaped elements have length p, cross-sectional area A_c and second moment of inertia J_c. The 'green' trusses have longitudinal stiffness equal to k_L. Diagonal 'violet' elements are mutually constrained to have the same displacement at the central point, where a hinge is introduced. The diagonal elements have cross-sectional area A_d and second moment of inertia J_d. In order to characterize the microstructure, we use the non-dimensional stiffness ratio parameter $\beta = k_L p/(E_m A_c)$ and we introduce the sectional area ratio $\omega = A_d/A_c$ between the cross-sectional area of the diagonal beams and the cross-sectional area of the arms of the cross-shaped elements. We choose to tune such coefficients to obtain a null Poisson's ratio in a isotropic structure.

The structure has been studied numerically with the finite element code *Comsol Multiphysics*®, referring to an elementary cell subjected to appropriate periodic boundary conditions. The calculations are performed considering a Young's modulus $E_m = 200000$ MPa, a length of the arms $p = 10$ mm and a circular cross-section with radius $r = 0.25$ mm. The constitutive behavior of the lattice, generally cubic, is a function of the two non-dimensional microstructural parameters β and ω, that can be tuned to give an isotropic behavior and a Poisson's ratio equal to zero.

To ensure isotropic behavior we start fixing the value of the non-dimensional parameter $\beta = 0.005$, and we modify the ratio ω comparing the effective

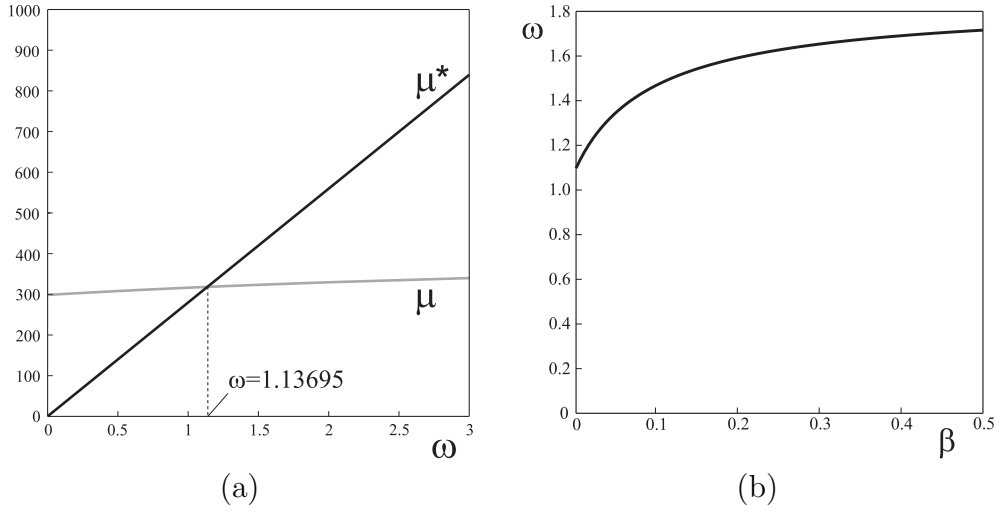

Figure 10: (a) In gray color: effective shear modulus μ as a function of sectional area ratio ω; in black color effective shear modulus μ^* in case of isotropic behavior. The curves are given for a stiffness ratio $\beta = 0.005$. The intersection point at $\omega = 1.13695$ represents the value of the shear modulus for which the lattice assumes isotropic behavior. (b) Sectional area ratio ω as a function of stiffness ratio β that assures isotropic behavior.

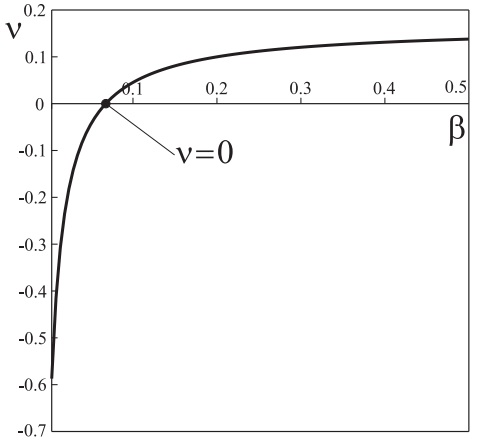

Figure 11: Poisson's ratio ν as a function of β, in case of isotropic behavior. For $\beta = 0.063$ the effective Poisson's ratio $\nu = 0$.

shear modulus μ with the shear modulus $\mu^* = E/(2(1+\nu))$ that the lattice would have in case of isotropic behavior. This comparison is shown in Fig. 10a, where the intersection point identifies the value $\omega = 1.13695$ for which the lattice has the desired isotropic behavior. Repeating this analysis for different stiffness ratios β it is possible to determine numerically the set of microstructural parameters (β, ω) that gives an effective isotropic behavior. Such a set is shown in Fig. 10b. The value of the Poisson's ratio as a function

of β for the isotropic structure is shown in Fig. 11. The Poisson's ratio for $\beta = 0.063$ is zero.

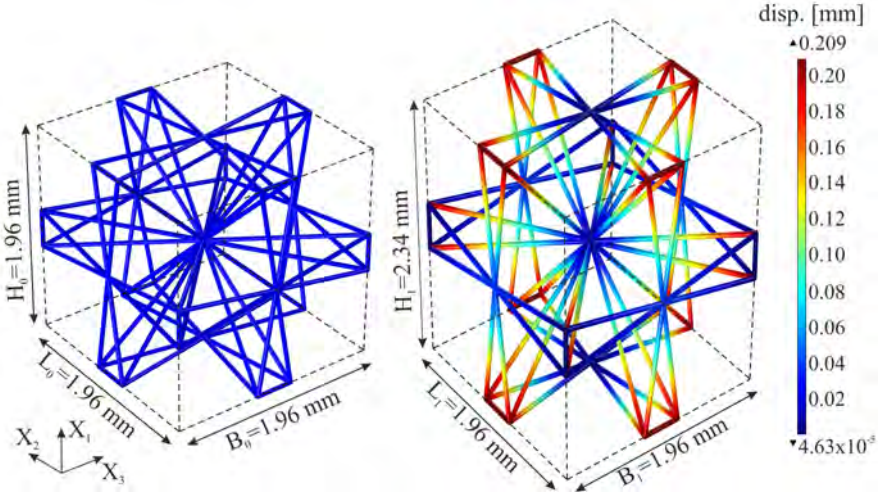

Figure 12: Deformation of the unit cell under an uniaxial load applied along the direction x_3. On the left the stress-free configuration, on the right the deformed unit cell.

In Fig. 12 we show the deformation of the isotropic lattice for the critical value of stiffness ratio $\beta = 0.063$. The deformation of a single unit cell is shown and it is given evidence that $\overline{\varepsilon}_{11} = \overline{\varepsilon}_{22} = 0$ when a stress component $\overline{\sigma}_{33}$ is applied, corresponding to $\nu = 0$.

4. Conclusion

This work describes the design of different microstructured media having a null Poisson's ratio. Both continuous and discrete structures have been proposed and the interplay between the geometry of the microstructure and the effective Poisson's ratio has been detailed. Such microstructures are sufficiently simple and they can be fabricated with existing technologies. We believe that these types of materials can find advanced applications in many fields, ranging from heat engines to actuators and energy transmission.

Acknowledgments

The authors acknowledge the financial support of Regione Autonoma della Sardegna, Italy (LR7 2010, Grant M4 CRP-27585).

References

Christensen, R.M., 1979. Mechanics of composite materials. Wiley-Interscience, New York.

Milton, G.W., 2002. The Theory of Composites. Cambridge University Press, Cambridge.

Bauer, J., Hengsbach, S., Tesari, I., Schwaiger, R., Krafta, O., 2014. High-strength cellular ceramic composites with 3D microarchitecture. *PNAS,* **111***(7), 2453-2458.* doi: 10.1073/pnas.1315147111

Jang, D., Meza, L.R., Greer, F., Greer, J.R., 2013. Fabrication and deformation of three-dimensional hollow ceramic nanostructures. *Nat. Mat.,* **12***, 893-898.* doi: 10.1038/nmat3738

Love, A.E.H., 1944. A treatise on the mathematical theory of elasticity, 4th edn. Dover Publications, New York.

Evans, K.E., 1991. Auxetic polymers: a new range of materials. *Endeavour,* **15***(4), 170-174.* doi: 10.1016/0160-9327(91)90123-S

Greaves, G.N., Greer, A.L., Lakes, R.S., Rouxel, T., 2011. Poisson's ratio and modern materials. *Nat. Mat.,* **10***, 823-827.* doi: 10.1038/nmat3134

Elipe, J.C.A., Lantada, A.D., 2012. Comparative study of auxetic geometries by means of computer-aided design and engineering. *Smart Mater. Struct.,* **21***, 105004.* doi: 10.1088/0964-1726/21/10/105004

Mir, M., Ali, M.N., Sami, J., Ansari, U., 2014. Review of Mechanics and Applications of Auxetic Structures. *Adv. Mater. Sci. Eng.,* **2014***, 753496.* doi: 10.1155/2014/753496

Milton, G.W., 2015. New examples of three-dimensional dilational materials. *Phys. Status Solidi B,* **252***(7), 1426-1430.* doi: 10.1002/pssb.201552297

Jardin, R.T., Fernandes, F.A.O., Pereira, A.B., Alves de Sousa, R.J., 2015. Static and dynamic mechanical response of different cork agglomerates. *Materials and Design,* **68***, 121-126.* doi: 10.1016/j.matdes.2014.12.016

Wu, Y., Yi, N., Huang, L., Zhang, T., Fang, S., Chang, H., Li, N., Oh, J., Lee, J.A., Kozlov, M., Chipara, A.C., Terrones, H., Xiao, P., Long, G., Huang, Y., Zhang, F., Zhang, L., Lepro, X., Haines, C., Lima, M.D., Lopez, N.P., Rajukumar, L.P., Elias, A.L., Feng, S., Kim, S.J., Narayanan,

N.T., Ajayan, P.M., Terrones, M., Aliev, A., Chu, P., Zhang, Z., Baughman, R.H., Chen, Y., 2015. Three-dimensionally bonded spongy graphene material with super compressive elasticity and near-zero Poissons ratio. *Nat. Comm.,* **6***, 6141.* doi: 10.1038/ncomms7141

Nguyen, C., Maheshwari, V., Saraf, R.F., 2012. Ultrasoft 100 nm Thick Zero Poissons Ratio Film with 60% Reversible Compressibility. *Nanoletters,* **12***(4), 2171-2175.* doi: 10.1021/nl300686c

Gibson, L.G., Ashby, M.F., 1997. Cellular Solids - Structures and Properties. Cambridge University Press, Cambridge.

Soman, P., Fozdar, D.Y., Lee, J.W., Phadke, A., Varghese, S., Chen, S., 2012. A three-dimensional polymer scaffolding material exhibiting a zero Poisson's ratio. *Soft Matter,* **8***, 4946-4951.* doi: 10.1039/C2SM07354D

Carta, G., Brun, M., Baldi, A., 2015. A design of a porous material with isotropic negative Poisson's ratio. *Submitted to Mech. Mater.*.

Cabras, L., Brun, M., 2014. Auxetic two-dimensional lattices with Poisson's ratio arbitrarily close to -1. *Proc. R. Soc. Lond. A,* **470***, 20140538.* doi: 10.1098/rspa.2014.0538

Capurso M., 1971. Lezioni di Scienza delle Costruzioni. Pitagora Editrice, Bologna.

Cabras, L., Brun, M., 2015. A class of auxetic three-dimensional lattices. *Submitted to J. Mech. Phys. Solids.*